THE EFFECT OF BLADE DEFORMATION ON ROTORCRAFT ACOUSTICS

Christopher C. Hennes* and Kenneth S.Brentner†
The Pennsylvania State University
University Park, Pennsylvania, U.S.A.

Abstract

The aeromechanical environment of rotorcraft is extremely complex, involving complex aerodynamics, rigid blade motion, and complex elastic deformation. Until recently rotorcraft noise prediction has included the rigid blade motions only, neglecting blade flexibility. Some recent research has attempted to include the effects of the elastic deformation, but this paper presents the first rigorous study of the impact of including flexibility on the acoustics. A derivation of Farassat's Formulation 1A is presented which includes two additional terms related to the surface deformation. The acoustics code PSU-WOPWOP has been modified to include these terms: several cases are analyzed and the impact of flexibility, including the effect of the changing surface area, is examined. The main case considered is a utility helicopter in high-speed forward flight. The aerodynamic inputs to the acoustics code were calculated using an elastic blade definition. The effect of making a rigid-blade approximation in the acoustics is investigated, and it is determined that the effect on thickness noise can be reduced by proper positioning of the blade tip. It is then shown that loading noise presents a larger challenge, and the rigid blade approximation can lead to significant errors at some observer locations. Finally, the thickness noise of a speculative advanced "smart materials" blade is examined to set an upper limit on the impact of the new formulation on rotorcraft acoustics. It is found that for present rotorcraft, the additional terms may be neglected safely, although the other effects of blade flexibility should be included.

Notation

$\Box^2$	d'Alembertian or wave operator, $\left[(1/c^2)(\partial^2/\partial t^2\right] - \nabla^2$
a	Mean sphere radius, m
c	Speed of sound (quiescent medium), ms^{-1}
dS	Differential element of surface area, m^2
$f=0$	Function that describes the integration surface (i.e. the rotor blade)
g	Retarded time function, $g = \tau - t + r/c$
H	Heaviside function, $H(f) = 0$ for $f < 0$ and $H(f) = 1$ for $f > 0$
J	Jacobian of transformation
ℓ_i	Components of loading force acting on the fluid, Nm^{-2}
ℓ_r	$\ell_i \hat{r}_i$, loading force in the radiation direction (summation implied), Nm^{-2}
ℓ_M	$\ell_i \hat{M}_i$ (summation implied), Nm^{-2}
$\dot{\ell}_r$	$\hat{r}_i \partial \ell_i / \partial t$ (summation implied), Nm^{-2} s^{-1}
M	Mach number of source, v/c
M_i	Components of the Mach number of the acoustic source, $M_i = v_i/c$
M_r	$M_i \hat{r}_i$, Mach number of source in radiation direction (summation implied)
$\hat{n}$	Outward-facing unit normal vector to surface $f=0$
p'	Acoustic pressure, $p - p_0$, Pa
p'_T	Thickness noise contribution to p', Pa
p'_L	Loading noise contribution to p', Pa
Q	Right-hand side term (source term) in an inhomogeneous wave equation
r	$\mathbf{x} - \mathbf{y}$, Distance between observer and source, m
t	Observer time, s
T_{ij}	Lighthill stress tensor
u_1, u_2	Time-independent coordinates on source surface Ω
v_n	$v_i \hat{n}_i$ (summation implied), Normal velocity of blade surface, ms^{-1}
$\dot{v}_n$	$\hat{n}_i \partial \hat{v}_i / \partial t$ (summation implied), ms^{-2}
$v_{\dot{n}}$	$v_i \partial \hat{n}_i / \partial t$ (summation implied), ms^{-2}
x_i	Observer location, m
y_i	Source location, m

Greek symbols

$\delta(f)$	Dirac delta function
μ	Advance ratio, ratio of forward flight speed to blade tip speed
ω	Pulsation rate, rad/s
Ω	Time-independent integration surface

*Graduate Research Assistant; chennes@psu.edu
†Associate Professor; ksbrentner@psu.edu

Presented at the 31st European Rotorcraft Forum, Florence, Italy, September 13–15, 2005.

ϕ Example dependent variable of an inhomogeneous wave equation

ρ_0 Density of quiescent medium, kg m^{-3}

τ Source time, s

Subscripts

a Quantity taken at the mean surface of the pulsating sphere

i i^{th} component of a vector

j j^{th} component of a vector

L Loading noise component

n Vector quantity taken in the surface normal direction, $\mathbf{x}\cdot\hat{n}$

r Vector quantity taken in the radiation direction, $\mathbf{x}\cdot\hat{r}$

ret Quantity evaluated at retarded time $\tau = t - r/c$

T Thickness noise component

Introduction

Helicopter noise has proven to be a persistent problem both for community acceptance of helicopters and heliports, and for military stealth requirements. Much of the research in the field of helicopter noise prediction has been focused towards developing tools that can be used at the design stage to identify the noise characteristics of helicopters based on CAD geometry inputs. In addition, over the past several years tools have been developed to study the noise generated by helicopters in arbitrary maneuvering flight. One of the challenges to this type of approach is that the aerodynamic environment of a helicopter is extremely complex even in steady flight conditions.

For a helicopter in maneuvering flight the blade motion is extremely complex: in addition to the motions of the helicopter (velocity, roll, pitch, yaw), the individual blades undergo time-dependent, aperiodic pitching, flapping and lead-lag. Finally, the rotor blades undergo significant elastic deformation in bending and torsion. Until recently most rotorcraft acoustics studies neglected the elastic motion of the blades. This seemed to be a reasonable approach since a large part of the impact of the blade elasticity is captured through elastic computation of the rotor blade aerodynamic loading.

Elastic blade motion can have a large impact on the rotor aerodynamics. If, for example, the blade twists under a load, the local angle of attack can differ substantially from that set by the rigid feathering motion of the blade and the twist built into the blade. This, in turn, will change the lift and drag distributions on the blade, as well as the shed vorticity and thus the blade wake. A blade that bends out of the rotor plane under load can easily move the tip position by over a chord length, affecting the position of tip vortices and in turn the orientation of future blade-vortex interactions. Any change to the aerodynamics will affect the acoustics through the loading noise term. It was assumed in most previous research that using blade loading calculations that include the flexible blade dynamics and aerodynamics would enable the acoustics code to capture most of the effect of the noise due to blade flexibility.

For example, if the acoustic input data was from an experiment, it was assumed (many times due to practical limitations on the amount of deformation information available) that the deformations could be neglected by the acoustics code, because the real, fully flexible blade aerodynamics were used to calculate the loading term. Note, however, that the loading noise is not a function of loading only, but the source position and the time derivative of the source position. Inclusion of accurate aerodynamics does not correct these source position and motion errors. Further, the noise in the rotor plane is primarily thickness noise, which depends strongly on the position, velocity, and acceleration of the the blade surface. These quantities are all modified by elastic deformations of the blade.

In recent years a few studies have been done that included the elastic deformation in the acoustics calculations (at least in an approximate way) [1, 2]. The results of these studies suggested that blade flexibility was important, but no systematic examination of the impact of including the blade deformations in the calculation has been conducted previously.

Derivation

An examination of the derivation of Formulation 1A reveals that the surface is assumed to be rigid, and thus any codes based on it have an implicit assumption that the geometry is not deforming as a function of time. In order to properly investigate the effect of blade deformation on acoustics calculations a new formulation is needed which relaxes the rigid body assumption.

The Ffowcs Williams–Hawkings (FW–H) equation is an exact rearrangement of the governing equations of fluid dynamics, so provides a suitable starting point for a new derivation:

$$\begin{aligned}\Box^2 p'(\mathbf{x},t) = &\frac{\partial}{\partial t}\left(\rho_o v_n \delta(f)\right)\\ &-\frac{\partial}{\partial x_i}\left(\ell_i \delta(f)\right)\\ &+\frac{\partial^2}{\partial x_i \partial x_j}\left(T_{ij} H(f)\right)\end{aligned} \tag{1}$$

This equation is an inhomogeneous wave equation for external flows, which through the use of generalized function theory, has been embedded in unbounded space. This enables the use of the free-space Green's function, $\delta(g)/4\pi r$ (where $g = \tau - t + r/c$), to find an integral representation to the solution.

Consider, for example, the inhomogeneous wave equation

$$\Box^2\phi(\mathbf{x},t) = Q(\mathbf{x},t)\delta(f) \tag{2}$$

which is in the generic form of the surface terms in the FW–H equation. Using the free-space Green's function, the integral representation of the solution can be written as

$$4\pi\phi(\mathbf{x},t) = \int_{-\infty}^{t}\int_{-\infty}^{\infty}\frac{Q(\mathbf{y},\tau)\delta(f)\delta(g)}{r}d\mathbf{y}d\tau. \tag{3}$$

To integrate the Dirac delta functions, a change of variables is required. Several different changes are possible: in this derivation the retarded-time transformation of $(\mathbf{y},\tau) \rightarrow (f,g,dS)$ is used (See Ref. [3] for analysis of several other possibilities). Care must be taken at this state to ensure that no assumption of rigid motion is made. The transformation is in two parts, $y_3 \rightarrow f$ and $\tau \rightarrow g$. Examining the y_3 transformation first,

$$\left|\frac{\partial f}{\partial y_3}\right| dy_3 = df \tag{4}$$

From an examination of the surface geometry it can also be seen that

$$dS = \frac{dy_1 dy_2}{\left|\frac{\partial f}{\partial y_3}\right|} \tag{5}$$

Using these two relations, Eq. 3 can be written

$$4\pi\phi(\mathbf{x},t) = \int_{-\infty}^{t}\int_{-\infty}^{\infty}\frac{Q(\mathbf{y},\tau)\delta(f)\delta(g)}{r}dSdfd\tau \tag{6}$$

This transform is mathematically exact, even if the surface $f = 0$ and area dS are functions of time. The next transformation is $\tau \rightarrow g$:

$$\left|\frac{\partial g}{\partial \tau}\right| d\tau = dg \tag{7}$$

It can then be shown that this Jacobian of transformation is $|\partial g/\partial\tau| = |1 - M_r|$. Substituting this into Eq. 6 yields

$$4\pi\phi(\mathbf{x},t) = \int_{-\infty}^{t}\int_{-\infty}^{\infty}\frac{Q(\mathbf{y},\tau)\delta(f)\delta(g)}{r|1-M_r|}dSdfdg \tag{8}$$

Integrating with respect to f yields

$$4\pi\phi(\mathbf{x},t) = \int_{-\infty}^{t}\int_{f=0}\frac{Q(\mathbf{y},\tau)\delta(g)}{r|1-M_r|}dSdg \tag{9}$$

Up to this point the derivation has followed Farassat's original derivation quite closely. The next step is to integrate with respect to g. Here, noting that dS is a function of τ, it is preferable to change variables to give an integration over a time-independent quantity. This can be accomplished by mapping the time-dependent integration surface $f = 0$ to a time-independent region Ω, with coordinates (u_1,u_2):

$$dS \equiv Jdu_1du_2 \tag{10}$$

where J is the Jacobian of transformation. This is similar to the method used by Farassat and Tadghighi in Ref. [4]. Eq. 9 can then be written

$$4\pi\phi(\mathbf{x},t) = \int_{-\infty}^{t}\int_{\Omega}\frac{Q(\mathbf{y},\tau)J\delta(g)}{r|1-M_r|}du_1du_2dg \tag{11}$$

The g integration can now be performed to give:

$$4\pi\phi(\mathbf{x},t) = \int_{\Omega}\left[\frac{Q(\mathbf{y},\tau)J}{r|1-M_r|}\right]_{\text{ret}}du_1du_2 \tag{12}$$

where the "ret" subscript indicates that the term in brackets is evaluated at the retarded time.

Returning to the FW–H equation (Eq. 1), it can be seen that, neglecting the quadrupole term, the surface terms are in nearly the form seen in Eq. 3, except for the additional time and space derivatives:

$$\begin{aligned}4\pi p'(\mathbf{x},t) =& \frac{\partial}{\partial t}\int_{\Omega}\left[\frac{\rho_0 v_n J}{r|1-M_r|}\right]_{\text{ret}}du_1du_2 \\ &-\frac{\partial}{\partial x_i}\int_{\Omega}\left[\frac{\ell J}{r|1-M_r|}\right]_{\text{ret}}du_1du_2\end{aligned} \tag{13}$$

Since the d'Alembertian $\Box^2$ is a linear operator, the operations commute and the FW–H equation can be rearranged and written in integral form (omitting the quadrupole term) as

$$\begin{aligned}4\pi p'(\mathbf{x},t) =& \frac{1}{c}\frac{\partial}{\partial t}\int_{\Omega}\left[J\frac{\rho_0 c v_n + \ell_r}{r|1-M_r|}\right]_{\text{ret}}du_1du_2 \\ &+\int_{\Omega}\left[J\frac{\ell_r}{r^2|1-M_r|}\right]_{\text{ret}}du_1du_2\end{aligned} \tag{14}$$

Comparing this to Farassat's Formulation 1,

$$\begin{aligned}4\pi p'(\mathbf{x},t) =& \frac{1}{c}\frac{\partial}{\partial t}\int_{f=0}\left[\frac{\rho_0 c v_n + \ell_r}{r|1-M_r|}\right]_{\text{ret}}\mathrm{d}S \\ &+\int_{f=0}\left[\frac{\ell_r}{r^2|1-M_r|}\right]_{\text{ret}}\mathrm{d}S\end{aligned} \tag{15}$$

it is clear that the only difference is the coordinate transformation $dS \rightarrow Jdu_1du_2$. The real difference in the formulations appears when the time derivative is brought inside the the integral, as in the derivation of Formulation 1A. It can be shown that

$$\left.\frac{\partial}{\partial t}\right|_{\mathbf{x}} = \frac{1}{1-M_r}\left[\left.\frac{\partial}{\partial\tau}\right|_{\mathbf{x}}\right]_{\text{ret}} \tag{16}$$

where the $|_{\mathbf{x}}$ implies that the observer position $\mathbf{x}$ is fixed during differentiation. Since the integration is over u_1 and

u_2, which are not time-dependent, the time derivative can be moved:

$$\begin{aligned} &4\pi p'(\mathbf{x},t) = \\ &\frac{1}{c}\int_\Omega \left[\frac{1}{1-M_r}\frac{\partial}{\partial\tau}\bigg|_{\mathbf{x}}\left(J\frac{\rho_0 c v_n + \ell_r}{r|1-M_r|}\right)\right]_{\text{ret}} du_1 du_2 \\ &+\int_\Omega \left[J\frac{\ell_r}{r^2|1-M_r|}\right]_{\text{ret}} du_1 du_2 \end{aligned} \tag{17}$$

It is clear that the presence of the J will result in two additional terms when the derivative is evaluated (one from $J\rho_0 c v_n$ and one from $J\ell_r$), resulting in a new dependence on $\partial J/\partial\tau$, which does not appear in Farassat's original formulation.

Thickness noise

Examining the first part of the first integral (the $\rho_0 c v_n$ term) and applying the chain rule to the derivative yields

$$\begin{aligned} &\frac{1}{c}\int_\Omega \left[J\frac{1}{1-M_r}\frac{\partial}{\partial\tau}\bigg|_{\mathbf{x}}\left(\frac{\rho_0 c v_n}{r|1-M_r|}\right)\right]_{\text{ret}} du_1 du_2 \\ &+\frac{1}{c}\int_\Omega \left[\frac{1}{1-M_r}\frac{\rho_0 c v_n}{r|1-M_r|}\frac{\partial J}{\partial\tau}\right]_{\text{ret}} du_1 du_2 \end{aligned} \tag{18}$$

The first integral is identical to the corresponding integral in Farassat's original Formulation 1A — only the second integral is new. Using Farassat's results for the first integral, the solution becomes

$$\begin{aligned} &\int_\Omega \left[J\frac{\rho_0(\partial v_n/\partial t)}{r|1-M_r|^2}\right]_{\text{ret}} du_1 du_2 \\ &+\int_\Omega \left[J\frac{\rho_0 v_n\left[r\dot{M}_r + c\left(M_r - M^2\right)\right]}{r^2|1-M_r|^3}\right]_{\text{ret}} du_1 du_2 \\ &+\int_\Omega \left[\dot{J}\frac{\rho_0 v_n}{r|1-M_r|^2}\right]_{\text{ret}} du_1 du_2 \end{aligned} \tag{19}$$

Comparing this to Farassat's result it can clearly be seen that the only change to his version of this term (the so-called "thickness noise" term) is the addition of an additional integral incorporating the time derivative of the Jacobian of transformation function J.

Loading noise

Next, examining the second part of the first integral in Eq. 17 (the ℓ_r term),

$$\frac{1}{c}\int_\Omega \left[\frac{1}{1-M_r}\frac{\partial}{\partial\tau}\bigg|_{\mathbf{x}}\left(J\frac{\ell_r}{r|1-M_r|}\right)\right]_{\text{ret}} du_1 du_2 \tag{20}$$

Again, splitting this integral into two parts via the chain rule,

$$\begin{aligned} &\frac{1}{c}\int_\Omega \left[J\frac{1}{1-M_r}\frac{\partial}{\partial\tau}\bigg|_{\mathbf{x}}\left(\frac{\ell_r}{r|1-M_r|}\right)\right]_{\text{ret}} du_1 du_2 \\ &+\frac{1}{c}\int_\Omega \left[\frac{1}{1-M_r}\frac{\ell_r}{r|1-M_r|}\frac{\partial J}{\partial\tau}\right]_{\text{ret}} du_1 du_2 \end{aligned} \tag{21}$$

This result again consists of integrals which correspond exactly to those in Farassat's derivation of Formulation 1A, and a new term due to the deforming surface. Using Farassat's result gives a new "loading noise" term:

$$\begin{aligned} &\frac{1}{c}\int_\Omega \left[J\frac{\dot{\ell}_r}{r|1-M_r|^2}\right]_{\text{ret}} du_1 du_2 \\ &+\frac{1}{c}\int_\Omega \left[J\frac{-c\ell_M + v_r\ell_r}{r^2|1-M_r|^2}\right]_{\text{ret}} du_1 du_2 \\ &+\frac{1}{c}\int_\Omega \left[J\frac{\ell_r c M^2 - r\ell_r\dot{M}_r}{r^2|1-M_r|^3}\right]_{\text{ret}} du_1 du_2 \\ &+\frac{1}{c}\int_\Omega \left[\dot{J}\frac{\ell_r}{r|1-M_r|^2}\right]_{\text{ret}} du_1 du_2 \end{aligned} \tag{22}$$

Formulation 1A – Flexible

The full version of Formulation 1A including the effects of blade flexibility is

$$\begin{aligned} &4\pi p'(\mathbf{x},t) = \\ &\int_\Omega \left[J\frac{\rho_0(\partial v_n/\partial t)}{r|1-M_r|^2}\right]_{\text{ret}} du_1 du_2 \\ &+\int_\Omega \left[J\frac{\rho_0 v_n\left[r\dot{M}_r + c\left(M_r - M^2\right)\right]}{r^2|1-M_r|^3}\right]_{\text{ret}} du_1 du_2 \\ &+\int_\Omega \left[\dot{J}\frac{\rho_0 v_n}{r|1-M_r|^2}\right]_{\text{ret}} du_1 du_2 \\ &+\frac{1}{c}\int_\Omega \left[J\frac{\dot{\ell}_r}{r|1-M_r|^2}\right]_{\text{ret}} du_1 du_2 \\ &+\frac{1}{c}\int_\Omega \left[J\frac{-c\ell_M + v_r\ell_r}{r^2|1-M_r|^2}\right]_{\text{ret}} du_1 du_2 \\ &+\frac{1}{c}\int_\Omega \left[J\frac{\ell_r c M^2 - r\ell_r\dot{M}_r}{r^2|1-M_r|^3}\right]_{\text{ret}} du_1 du_2 \\ &+\frac{1}{c}\int_\Omega \left[\dot{J}\frac{\ell_r}{r|1-M_r|^2}\right]_{\text{ret}} du_1 du_2 \end{aligned} \tag{23}$$

It has two integrals in it which do not appear in the original version of Formulation 1A, both involving the time derivative of the Jacobian of transformation, and the original integrals have been re-written in terms of u_1 and u_2. This Jacobian can be found from

$$\left|\frac{\partial u_i}{\partial s_i}\right| ds_i = du_i \tag{24}$$

where the s_i are the original surface coordinates for $i = 1,2$ and du_i are the transformed coordinates. This then gives

$$J = \frac{1}{\left|\frac{\partial u_1}{\partial s_1}\right|\left|\frac{\partial u_2}{\partial s_2}\right|} \tag{25}$$

Physically, this quantity is the ratio of the area of the original differential panel element dS to the area of the new panel element $du_1 du_2$. In a numerical implementation

each panel is of finite size. In this case, if the coordinates u_1 and u_2 range from $0 \rightarrow 1$ then the Jacobian J is just the area of the panel, and $\partial J/\partial \tau$ the time-rate of change of that panel area.

Results

It has been suggested previously [1, 2] that blade flexibility may play an important role in helicopter acoustics, but this role has never been well quantified. A new version of Formulation 1A has been derived and implemented in PSU-WOPWOP. This section presents several results using the new code. First, a case aimed at validation is presented, followed by an examination of the impact of blade deformation on a modern helicopter, and on a speculative future blade concept with large time-dependent chord and camber deformations.

Pulsating sphere

The pulsating sphere is a well-known acoustic problem, representative of a monopole source when the sphere is stationary. The first set of results is for a pulsating sphere where the radius is uniform at every point on the surface, but changes as a simple harmonic function of time. Two test cases are analyzed: the first uses a small-amplitude sinusoidal pulsation to compare to theoretical results derived by Dowling [5], and the second case uses a large-amplitude sinusoidal pulsation to examine the effect of the changing area (which is not included in Dowling's analytical results).

Small-amplitude pulsation Because it has been extensively studied analytically the pulsating sphere is a good test case to validate the new formulation with area change. All analytical results found during the course of this research, however, make assumptions about the sphere which are equivalent to the constant-area assumption, so the first case which is analyzed here is the small-amplitude case, since this should closely match known analytical results. For this case the maximum deflection of the sphere's surface is 1% of the radius, with an observer location at $10a$. Dowling's equation is used to calculate the pressure at the surface of the sphere. PSU-WOPWOP is then used to calculate the total sound propagation to the observer location.

Dowling's equation for the pressure at a radial distance r from a compact pulsating sphere source is

$$p'(r,t) = \frac{a^2}{r}\rho_0 \frac{\partial u_a}{\partial t}\left(t - \frac{r-a}{c}\right), \qquad \frac{\omega a}{c} << 1 \quad (26)$$

where a is the sphere's average radius and u_a is the radial velocity at the sphere's surface. The assumption of compactness means that the mean radius a is used as the radius at all times, and that the radiation vector r is constant, and measured from the center of the sphere. In

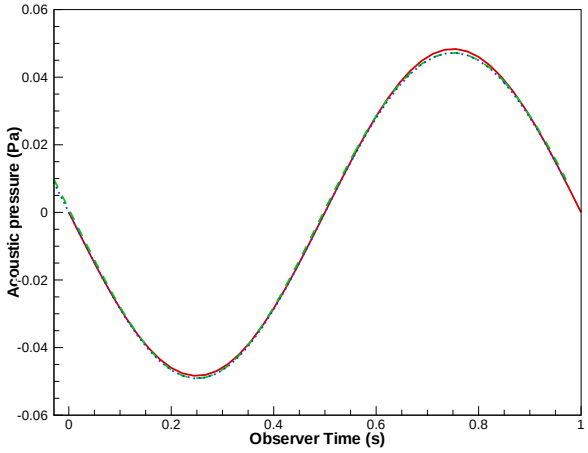

Figure 1: Small-amplitude pulsation: comparison of Dowling's formulation (——) with PSU-WOPWOP (– – –), and PSU-WOPWOP without the dJ/dt term (· · · · · ·).

PSU-WOPWOP both of these assumptions are relaxed: the radius of the sphere changes as a function of time, and the radiation vector is calculated at each timestep for each point on the sphere's surface. In the small-amplitude case analyzed here, $\omega = 1$ cycle/s, $a = 1.0$ m and $c = 342$ m/s. The pulsation amplitude is 0.01 m, or 1% of the sphere's radius, so the sphere is expected to behave nearly as a compact source.

Figure 1 shows the results for the small-pulsation case. As expected, the PSU-WOPWOP prediction is very close to the noise predicted by Dowling's compact formulation. The small downward shift of the PSU-WOPWOP results is due to the changing radiation vector in Formulation 1A — the effects of the area change are negligible in this case.

Large-amplitude pulsation The next case is identical to the previous case except that the pulsation amplitude is increased to 25% of the sphere's radius. The loading on the surface of the sphere is still approximated using Dowling's formulation at the average surface location. The results are plotted with those predicted by Dowling's equation at $r = 10a$ to demonstrate the departure from the approximate theoretical results as the effect of changing area and source location becomes more important.

Figure 2 shows the results for the non-compact case. There are two primary causes for the dramatic difference between these results. First, PSU-WOPWOP correctly models the changing radiation vector as the sphere's size changes: this effect is neglected in Dowling's formulation (as well as all other known formulations). In addition, the surface area of the sphere is changing significantly, increasing the importance of the new formulation which includes this effect.

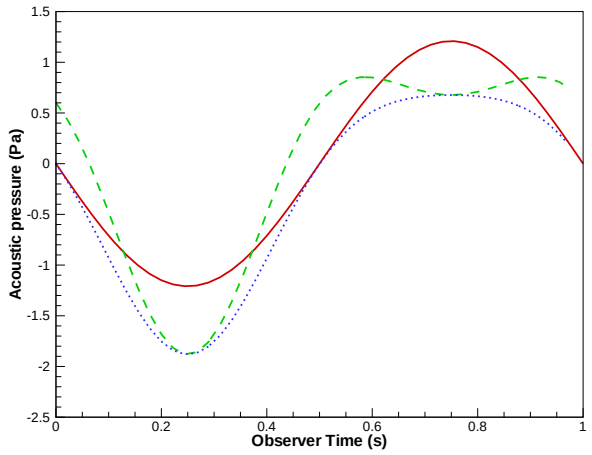

Figure 2: Large-amplitude pulsation: comparison of Dowling's formulation (——) with PSU-WOPWOP (– – –), and PSU-WOPWOP without the dJ/dt term (·····).

The shape of the signal calculated by Dowling's formulation maintains its perfect sinusoidal form, completely neglecting any change due to what is essentially a moving source. The formulation which neglects the dJ/dS term has a distorted sinusoidal shape, as it takes into account the changing source position, resulting in a larger amplitude when the sphere's radius is largest (and the sources therefore closer to the observer) and a smaller amplitude when the radius is smallest. Including the effects of the time-rate of area change then further distorts the sine wave, adding to the signal where the rate is highest, but matching the non-dJ/dt results when the time-rate of area change is zero (at the peaks of the wave).

Flexible rotor blade

A helicopter in high-speed forward flight is analyzed next. This case provides a large time-variation in the blade deformation, although the actual deformation distances involved are relatively small compared to a hover case. The purpose of this case is to determine the mechanisms through which the deformation affects the noise, and to evaluate the appropriateness of the usual approximation of including only the rigid blade motions when calculating helicopter acoustics.

The blade motions were calculated using CAMRAD [6]. These motions were then input into OVERFLOW [7, 8] to calculate the aerodynamic loads. Because OVERFLOW used the deformed blade coordinates at every timestep, the aerodynamic loading reflects the influence of the blade flexibility (Note that the CAMRAD simulation modeled only twist and bending deflections, and did not include the effects of changing blade cross-sections, which should be negligible).

Using the airloads calculated from the CFD, two acoustics cases were then run: the first by inputting only the rigid blade motion into the acoustics calculation, and the second including the full elastic blade motions. The rigid blade motion was determined by examining the flap, pitch, and lead-lag angles at the hinge locations. In both cases the aerodynamic computations reflect the loading for the case with elastic deformation.

Thickness noise on an observer plane The first results shown are for a plane of observers located $28.7R$ below the rotor. The observers are moving along with the rotor, as in a wind-tunnel test. Figure 3a shows the Overall Sound Pressure Level (OASPL) due to the thickness noise in the baseline rigid case. Figure 3b shows the change in noise due to the inclusion of the blade deformation, $\text{OASPL}_{\text{flexible}} - \text{OASPL}_{\text{rigid}}$. The circle in the figures represents the projection of the rotor onto the measurement plane.

Thickness noise is primarily directed in the rotor plane, so the levels seen in these plots are extremely low. Although the change in OASPL due to the inclusion of the flexibility seems large (up to 10dB at some positions), it is impossible to make a clear statement about the effect of the flexibility on the thickness noise at these positions because of the extremely low levels involved. A different distribution of observers is required to see the changes in thickness noise clearly. This will be addressed in a later section.

Loading noise on an observer plane The effect of the blade flexibility on the loading noise is much clearer on this plane because the overall levels are higher. Figure 4a shows the baseline rigid loading noise and Figure 4b shows the change due to the inclusion of flexibility.

The loading noise shows an increase in the region behind the rotor, from no change directly under the rotor to a 3dB increase 45° out of the rotor plane. This change occurs in a region where the levels are nearly 20dB below the peak level, however. There is also a general decrease in the levels on the measurement plane ahead of the rotor on the retreating side. None of these changes appear to be simple changes in the directivity of the noise: if they were directivity changes one would expect to see a region of increased noise near a similar region of decreased noise. No such patterns are evident in the loading noise on this plane. Figure 5a shows the total noise on the plane and Figure 5b shows the change in total noise. The total noise also shows a maximum difference of approximately 3dB.

Figures 5a and 5b are nearly identical to the loading noise plots as thickness noise has very little impact on a plane below the rotor. It appears that the predominant effect of the inclusion of blade flexibility is *not* a change in the noise directivity, but a change in the actual level of noise, at least on a plane below the rotor. In certain lo-

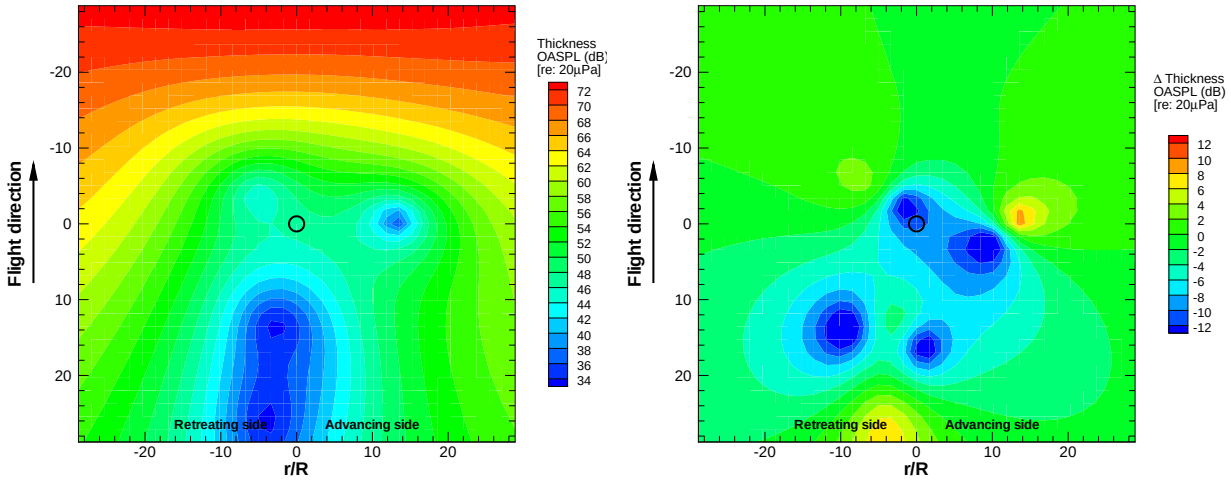

(a) Directivity for the baseline rigid blade case.

(b) Directivity change when flexibility is included.

Figure 3: Thickness noise OASPL on a plane below the rotor.

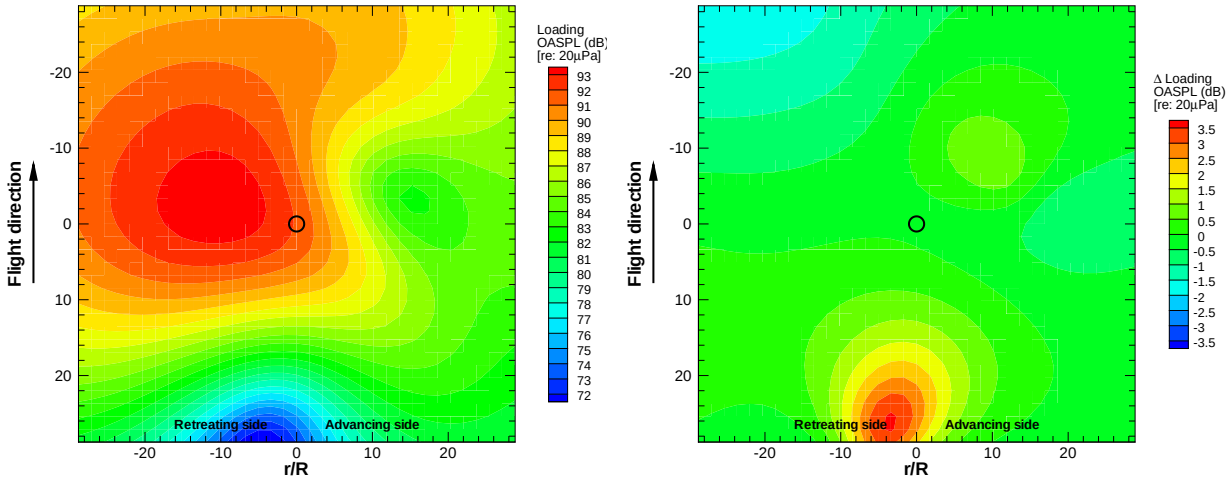

(a) Directivity for the baseline rigid blade case.

(b) Directivity change when flexibility is included.

Figure 4: Loading noise OASPL on a plane below the rotor.

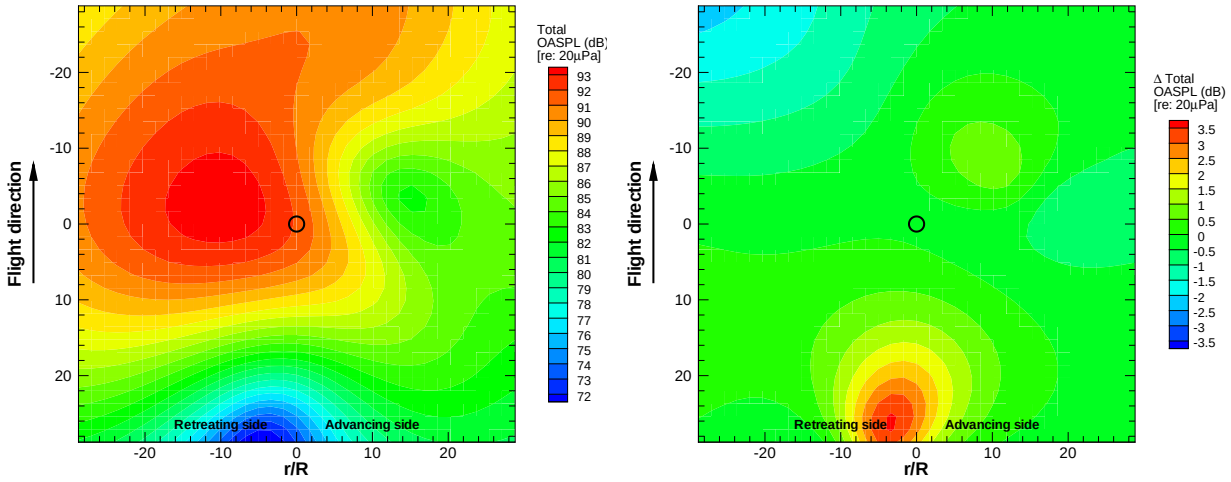

(a) Directivity for the baseline rigid blade case.

(b) Directivity change when flexibility is included.

Figure 5: Total noise OASPL on a plane below the rotor.

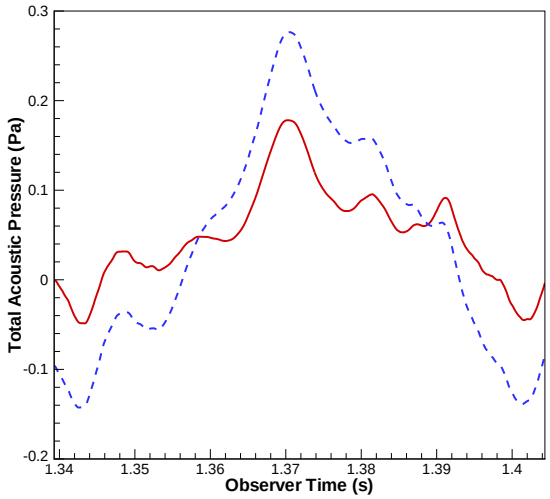

Figure 6: Total noise signal comparison at 26R behind and 3R to the retreating side, 28R below the rotor, for one blade passage. Rigid (——) and elasic (– – –) cases.

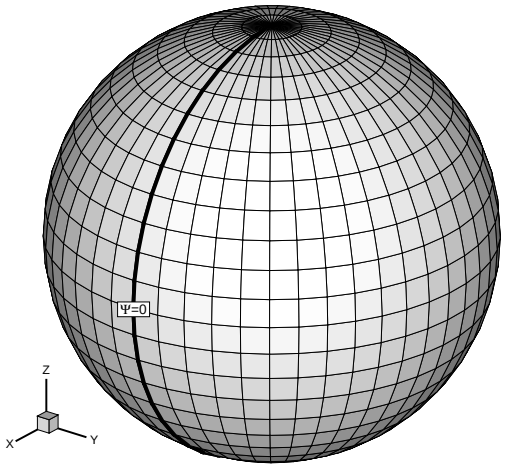

Figure 7: Layout of observer positions surrounding the rotor at $2.87R$.

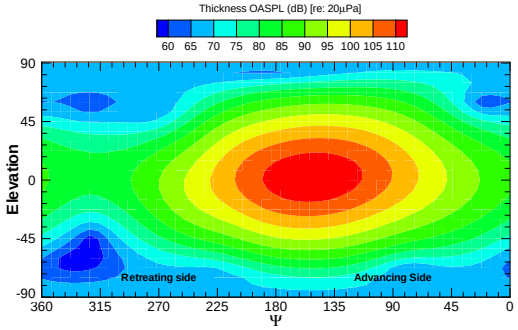

Figure 8: Thickness noise OASPL for a sphere of observers at $2.87R$.

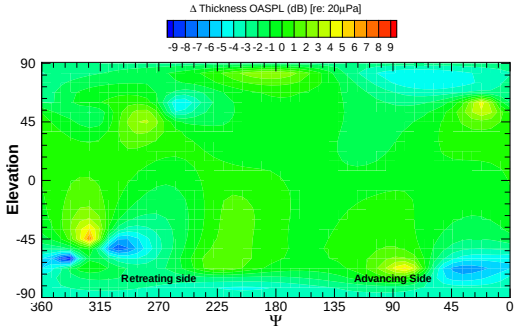

Figure 9: Change in thickness noise OASPL for a sphere of observers at $2.87R$.

cations this can be a substantial difference, but the overall directivity plot differs little between the two cases. To further investigate this effect, the acoustic pressure time history at the position of the largest OASPL change is shown for one blade passage in Figure 6. While the overall shape of the pressure signal is the same between the rigid and elastic cases, the elastic signal is much larger, resulting in the 3dB increase in OASPL seen in the directivity plot at this location. The higher harmonic content of the signal is due to fluctuations in the surface pressure calculated by the CFD. It is unknown whether these fluctuations are real, or artifacts of the numerical calculations. It is clear that care must be take in comparing the OASPL, and especially the pressure signal, at individual microphone locations. If flexibility is not included in the acoustics codes, significant departures from the true signal are possible in isolated locations, although these departures are frequently largest in regions where the noise level is much lower than the peak level, and may not be important acoustically. It is not know if this will always be the case. Nevertheless, small changes occur nearly everywhere.

Thickness noise directivity

To further understand the effects of blade flexibility, another set of observers was created. A spherical arrangement of observers was placed in the at $2.87R$. The observers move with the helicopter, so directivity and magnitude effects can be analyzed by examining the OASPL as a function of elevation and azimuth angle – observer distance is not a factor. Figure 7 shows the arrangement of the observers. The azimuth angle $\Psi = 180^\circ$ is ahead of the rotor, with 90° at the advancing side and 270° at the retreating side. The elevation angle is defined such that -90° is directly below the rotor, 0° is in the rotor plane, and 90° is directly above the rotor.

Figure 8 shows the OASPL due to the thickness noise as a function of azimuth angle, Ψ, and elevation angle, θ. As expected, the thickness noise plays a much larger role in the rotor plane, between -45° and 45° elevation. Figure 9 shows the difference between the rigid and the

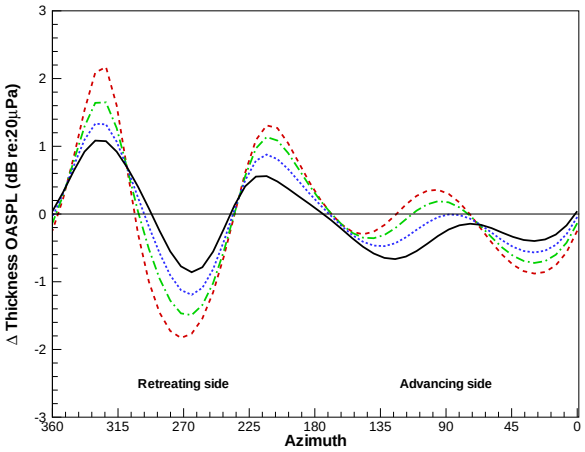

Figure 10: Change in thickness OASPL at four elevation angles in and below the rotor plane. In-plane (——), 7° below the plane (·····), 14° below the plane (—·—), and 21° below the plane (– – –).

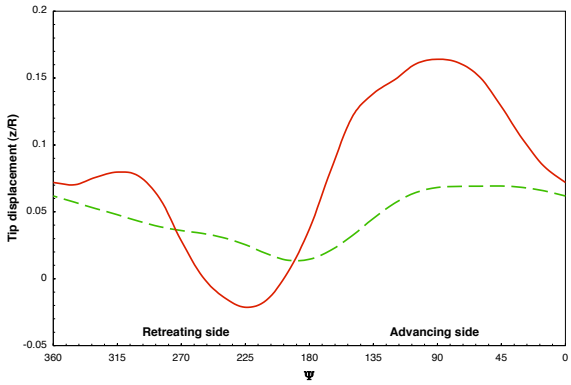

Figure 11: Out-of-plane tip deflections for the rigid (——) and elastic (– – –) cases.

flexible cases. As with the plane of observers, the overall change can be very large (up to 9dB), but the largest changes are located in the region where the thickness noise is of less importance. The large region in the rotor plane where the thickness noise is most important appears to have little change when viewed over this range of magnitudes (±9dB). Examining the change as a function of azimuth angle at several individual elevations sheds some insight into the effect of the flexibility on the thickness noise, however.

Figure 10 shows the change in thickness OASPL at four individual elevations near the rotor tip-path plane, where the thickness noise is most important. This plot indicates that even in the plane of the rotor (which in the previous directivity plot did not show much change) the thickness noise can change up to 1dB. The shift also shows a sinusoidal character with a lower amplitude on the advancing side and a higher amplitude on the retreating side. Figure 11 shows the blade tip out-of-plane deflection for the elastic and rigid cases. The blade deflections are largest on the advancing side, as is the difference in deflection between the rigid and elastic case, so this result seems counterintuitive. An investigation of the terms in the FW-H equation shows that the effect is primarily due to a difference in $\dot{M}_r$, from

$$\int_\Omega \left[\frac{J\rho_0 v_n \dot{M}_r}{r\left(1-M_r^3\right)}\right]_{\text{ret}} du_1 du_2 \qquad (27)$$

and more specifically, a change in the radiation vector r which, when dotted with $\dot{M}$, results in the sinusoidal variation in Thickness OASPL. This difference in $\dot{M}_r$ is largest at the retreating side, corresponding to the observed increase in ΔOASPL in that region. So, while the actual blade position difference is smaller at the retreating side than on the advancing side, $\dot{M}$ is larger, making up for the difference and resulting in a change in thickness OASPL that is larger in the fourth quadrant, at the retreating side.

The end result of this analysis is that the change in in-plane thickness noise is due to a change in the radiation vector at the tip of the blade — the change in normal vector direction does not appear to have a strong impact on the acoustics, despite a significant change in normal direction due to blade twisting, and the normal vector appearing in all of the thickness noise terms through v_n:

$$\begin{aligned} p'_T = &\int_\Omega \left[J\frac{\rho_0(\partial v_n/\partial t)}{r|1-M_r|^2}\right]_{\text{ret}} du_1 du_2 \\ &- \int_\Omega \left[J\frac{\rho_0 v_n\left[r\dot{M}_r + c\left(M_r - M^2\right)\right]}{r^2|1-M_r|^3}\right]_{\text{ret}} du_1 du_2 \\ &+ \int_\Omega \left[j\frac{\rho_0 v_n}{r|1-M_r|^2}\right]_{\text{ret}} du_1 du_2 \end{aligned} \qquad (28)$$

This leads to the suggestion that the primary non-aerodynamic effect of blade flexibility on thickness noise can be modeled using a rigid blade approximation if, rather than using the blade flapping angle at the flap hinge to describe the rigid blade motion, the flapping angle in the rigid case is set such that the blade tip position is the same in the elastic and rigid cases. Figure 12 shows a comparison of four different methods of calculating the thickness noise at the position of the largest difference in OASPL on the observer sphere. In addition to the baseline rigid and elastic cases, two additional rigid blade approximations are made. The first case uses a blade flapping angle calculated such that the out-of-plane displacement of the blade tip matches that in the elastic case. The second case uses that flap angle, and in addition calculates the blade feathering angle such that the angle of attack at the tip of the rigid blade corresponds to that in the elastic blade. A clear improvement to the signal is shown when the adjusted flapping places the blade tip

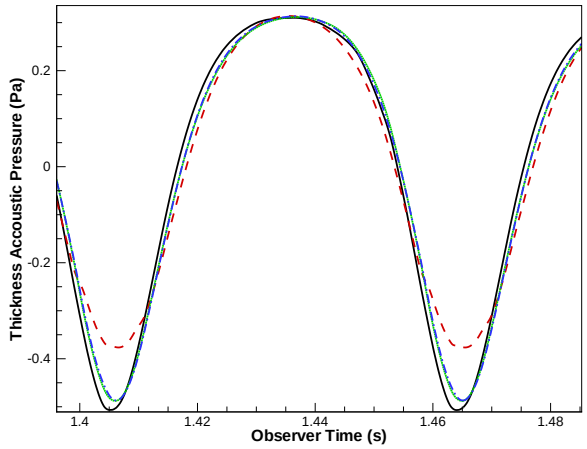

Figure 12: Comparison of thickness noise calculated with the fully elastic formulation (———), rigid blades with the original inputs (– – –), rigid blades with matching out-of-plane tip displacement of the elastic case (·····), and rigid blades matching the displacement and tip angle of attack of the elastic case (—·—).

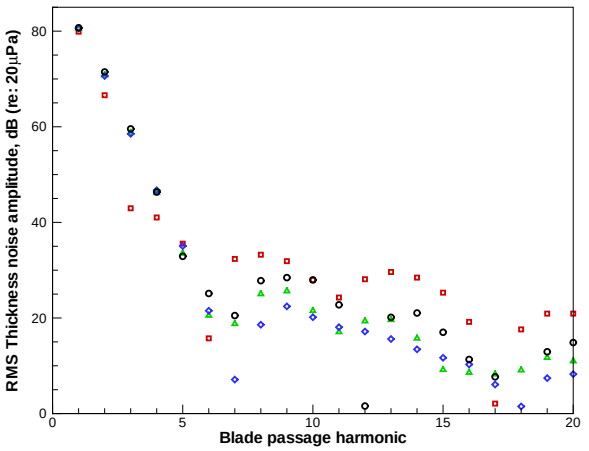

Figure 13: Comparison of thickness noise spectrum calculated with the fully elastic formulation (○), rigid blades with the original inputs (□), rigid blades with matching out-of-plane tip displacement of the elastic case (△), and rigid blades matching the displacement and tip angle of attack of the elastic case (◊).

in the correct position: the negative peak is much closer to the elastic case. This is due to the importance of the tip in the thickness noise calculations: because the velocity is highest at the tip, most of the thickness noise is generated in that region. If the tip position is correct, the thickness noise should be correct.

Figure 13 shows the spectrum calculated for this case. The spectrum shows that the lower harmonics improve significantly with the inclusion of the more advanced tip motions, and the feathering motions, while not affecting the first few harmonics, improve the prediction at some of the higher harmonics.

Loading noise directivity Figure 14 shows the OASPL due to the loading noise as a function of azimuth angle, Ψ, and elevation angle, θ. In the rotor plane the loading noise is very low, increasing as the angle out-of-plane increases. Figure 15 shows the difference between the rigid and the flexible cases. While the figure shows extremely large ΔdB differences between the two cases, including a clear directivity shift aft of the rotor at 330°, these in-plane differences are acoustically less significant since the loading noise is much larger out-of-plane. Figure 16 shows the change in loading OASPL as a function of azimuth at several elevation angles below the plane of the rotor. This figure shows a clear correspondence to Figure 10, except that the change is of opposite sign, and the thickness OASPL levels show an overall decrease at most locations. For the loading noise, however, the source of the change is not as easy to characterize directly. Careful examination of the individual terms' importance to the change in loading noise reveals that for this

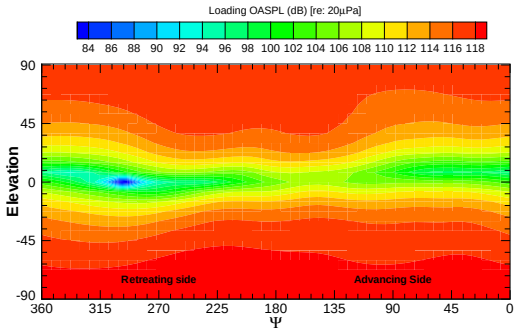

Figure 14: Loading noise OASPL for a sphere of observers at $2.87R$.

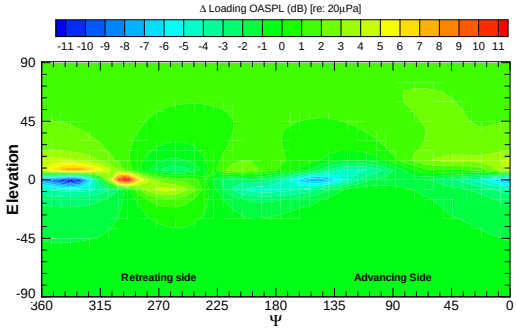

Figure 15: Change in loading noise OASPL for a sphere of observers at $2.87R$.

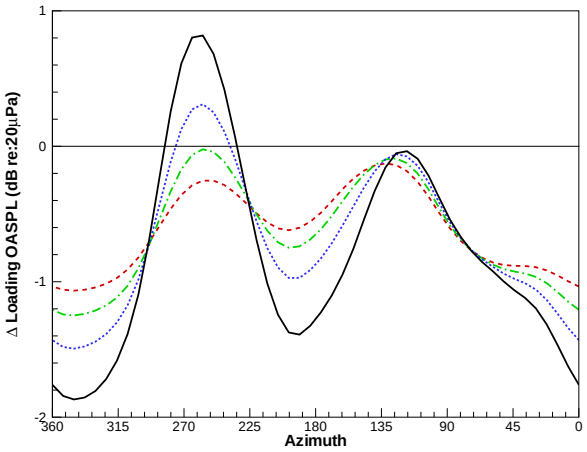

Figure 16: Change in loading OASPL at four elevation angles below the rotor plane. 21° below the plane (——), 28° below the plane (·····), 35° below the plane (—·—·), and 42° below the plane (— — —)

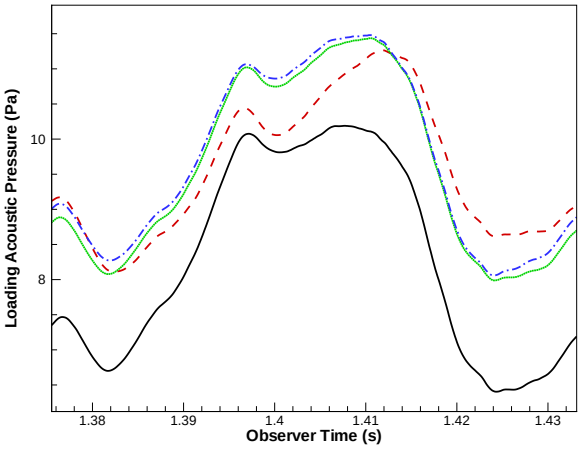

Figure 17: Comparison of loading noise calculated with the fully elastic formulation (——), rigid blades with the original inputs (— — —), rigid blades with matching out-of-plane tip displacement of the elastic case (·····), and rigid blades matching the displacement and tip angle of attack of the elastic case (—·—·).

near-field observer position, the predominant effect is still that of a changing radiation vector, rather than the changing normal vector, but the effect is far less pronounced than for the thickness case.

Figure 17 shows the effect on acoustic pressure of including more advanced tip approximations. The observer is located at the position of the largest change in loading noise seen on the observer sphere. Unlike in the thickness case (Figure 12), the loading noise calculation does not improve with the improved tip position. This is due to the fact that the loading noise generation is not neccessarily concentrated at the tip, and in this case is primarily produced at positions further inboard on the blade, between approximately $r/R = 0.75$ and $r/R = 0.9$. Figure 18 shows the total noise spectrum first 20 harmonics of the blade-passage frequency. Despite the significant differences in the pressure signal between the cases, the spectrum shows an improvement with the inclusion of the more refined rigid blade motions (matching the elastic geometry at the tip rather than the root). The exception is at the eighth harmonic of the blade passage frequency, where the more advanced blade motions give increased divergence from the fully elastic result.

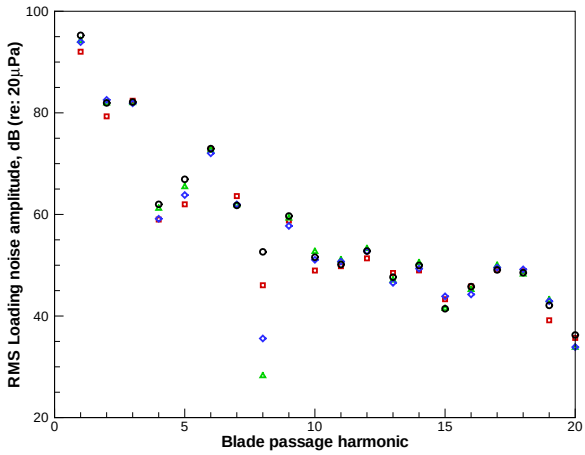

Figure 18: Comparison of loading noise spectrum calculated with the fully elastic formulation (○), rigid blades with the original inputs (□), rigid blades with matching out-of-plane tip displacement of the elastic case (△), and rigid blades matching the displacement and tip angle of attack of the elastic case (◊).

Active morphing rotor blade

The final set of results is a speculative study of the effects of very large surface deformation on the acoustics. A rotor blade whose cross-section changes as a function of time is modeled in high-speed forward flight. This case provides a study of the largest reasonable impact of the new changing-area formulation on rotorcraft noise. Larger area changes may be possible for a micro unmanned aerial vehicle (MAV), but this is left as a topic for future research now that the capability to include the

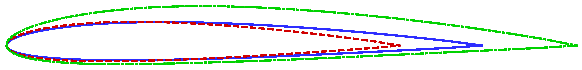

Figure 19: Non-deforming blade geometry (——), maximum extent of deforming blade geometry (—·—), and minimum extent of deforming blade geometry (– – –).

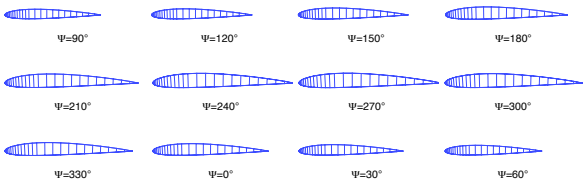

Figure 20: Morphing blade cross-section as a function of azimuth angle.

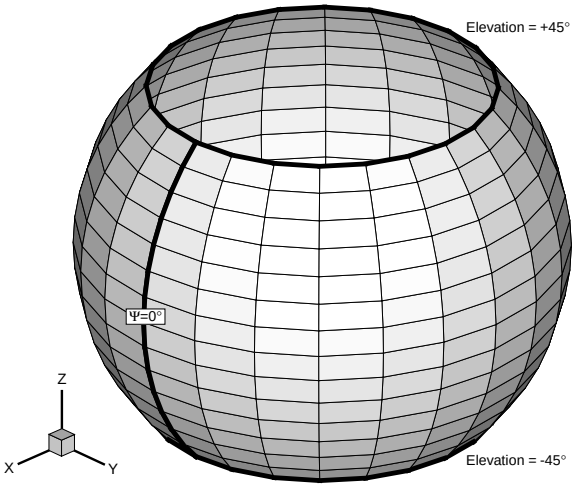

Figure 21: Arrangement of observers for the morphing blade analysis.

effect is available.

Figure 19 shows the extent of the geometry deformation, and figure 20 shows the morphing blade shape as a function of Ψ. This models an advanced rotor blade whose thickness and camber increase on the retreating side and decrease on the advancing side. While no rotors of this type exist at present, researchers are actively investigating "smart materials" which can produce deformations of the kind envisioned here [9,10]. It is expected that this case provides an example of the maximum reasonable area change for a rotor blade, and allows the isolation of area-change effects from the other acoustic affects presented in the previous section.

Only the thickness noise is examined for this case: no blade loading data is available for a geometry of this kind. Figure 21 shows the layout of observers, arranged in the elevation range $\pm 45^\circ$ of a sphere around the rotor.

Two cases are run for comparison. In the first case, a baseline, non-morphing geometry is run in high-speed forward flight. In the second case the morphing geometry is run in the same flight condition. Figure 19 shows the airfoil geometry for the two cases. Figure 22 shows the thickness noise OASPL for the baseline non-morphing case. Figure 23 shows the change when the morphing blade is included. As expected, the thickness noise decreases on the advancing side, where the blade is smaller than the baseline blade, and increases on the retreating side, where the blade is larger. On average the blade is larger than the baseline, so the general levels increase as well.

Next, the effect of the changing area term is investigated. A single observer position is examined in the rotor plane at $\Psi = 330^\circ$, 3R from the rotor hub. This is the area that shows the largest increase in thickness OASPL in the directivity plots. Figure 24 shows the acoustic pressure results for this position for three cases: the baseline rigid case, the full elastic formulation, and the elastic formulation with the dJ/dt term omitted. Clearly the baseline case misses the majority of the noise, due to the very thick airfoil used at this position in the deforming case, which is not properly modeled by the non-deforming blade. In addition, at this observer position the dJ/dt term has a relatively strong impact on the acoustic pressure time history. It can be expected that for a geometry with extremely large deformations, such as a MAV modeled after a bird undergoing a "spanning" motion (a change in wing chord), this term will be important to the acoustics calculations. For a more typical helicopter rotor, however, the effect is thought to be negligible as in the cases considered here.

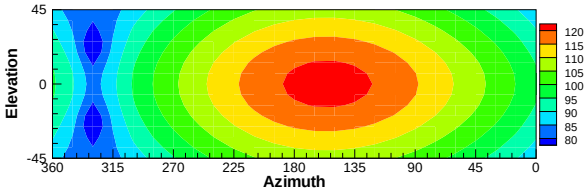

Figure 22: Baseline thickness OASPL (dB re:20μPa).

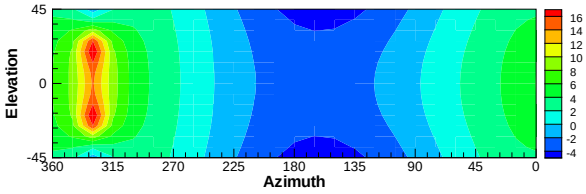

Figure 23: Change in thickness OASPL (dB re:20μPa).

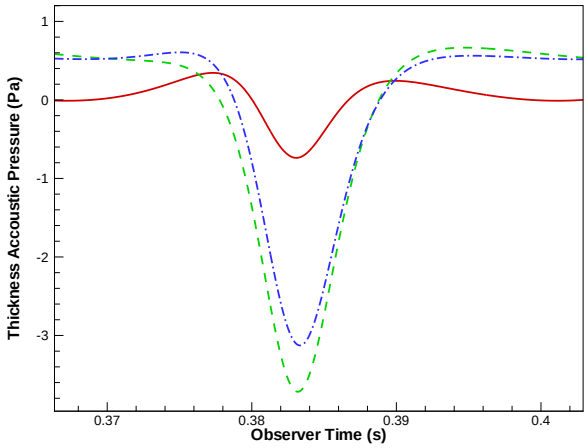

Figure 24: Comparison of baseline acoustic pressure (——), fully elastic acoustic pressure (– – –) and the elastic case calculated without the dJ/dt term (—·—).

Conclusion

Over the past several decades, researchers have been calculating rotorcraft acoustics using a rigid blade approximation. While these predictions have been quite successful, higher fidelity results are always desirable, especially if the computation cost is low. A new derivation of Formulation 1A is presented which does not include any assumptions of rigid geometry. This formulation includes two new terms, one in the thickness noise and one in the loading, reflecting the time rate of surface area change. PSU-WOPWOP has been modified to include a time-dependent surface geometry, and to implement this new formulation.

Several cases have been presented showing the effect of blade deformation on the acoustics, independent of any changes to the aerodynamics. In the high-speed forward flight case analyzed, substantial differences in both the thickness and loading noise were demonstrated. Differences in Total Noise OASPL of over 3dB were shown to occur at isolated observer locations. The largest OASPL differences were observed where the noise levels were much lower than the peak level, but differences of up to 1dB were observed in regions with levels nearer to the peak level. When analyzing the acoustic pressure time history directly, small changes due to flexibility are evident nearly everywhere, with much larger differences at isolated locations. It is not known whether the tendency for the largest changes to occur in the regions with the lowest levels is a general trend, or is particular to this case.

The prediction of thickness noise near the rotor tip-path plane for rigid rotor blades can be improved by matching the blade tip position rather than the blade angles at the root. In this case, the thickness noise calculated using a rigid-body simulation is quite close to the thickness noise calculated using the fully elastic geometry. The same method showed some improvement in the spectrum calculated for the out-of-plane loading noise, but did not have a positive effect on the the loading component of acoustic pressure time history or the OASPL.

Finally, to quantify the significance of the new terms introduced into Formulation 1A, a speculative morphing-blade rotor was investigated. Even in the case of extremely large blade deformations, the peak acoustic pressure differs by only 15% with the inclusion of the new terms. Based on this result, it is expected that the terms are negligible for conventional rotor noise predictions. However, this may not be true in the case of micro-aerial vehicles (MAVs) modeled after birds or insects. In those cases, extremely large elastic deformations may require the new formulation. The computational requirements for including the new terms are very low, so it may be worthwhile to include them in current acoustics codes to allow for the possibility of modeling large deformations should it become necessary.

Further investigation into the effects of deformation is needed to fully understand the limits of the rigid-blade approximation. The cases presented in this paper were for high-speed forward flight: it is expected that in some flight conditions the rigid-blade approximation may be more appropriate than in others. Furthermore, the examination of the time-rate of area change was limited to thickness noise results. Advanced CFD packages are capable of calculating the surface loading on this type of geometry, so that analysis should be expanded to include the loading noise. Finally, the additional terms may have a large importance in the calculation of noise generated by biologically-inspired MAVs. Some types of birds use an expansion and contraction of their wing surfaces as part of their flapping motions. These motions will clearly require the more advanced formulation.

Acknowledgments

The authors wish to thank Earl Duque, Jan Theron and Bryan Flynt for their OVERFLOW assistance. This research was sponsored by NASA Langley Research Center, Contract Monitor D. Doug Boyd. Contract number NNL05AD50P, NASA Langley Research Center.

References

1. D. Patt, L. Liu, and P. P. Friedmann. Rotorcraft vibration and noise prediction using a unified aeroelastic analysis. In *AIAA Paper 2003-1785, 44th AIAA/ASME/ASCE/AHS Structures, Structural Dynamics, and Materials Conference*, Norfolk, Virginia, April 7–10 2003.

2. Li Liu, Dan Patt, and Peretz P. Friedmann. Active vibration and noise reduction in rotorcraft using and aeroelastic simulation. In *American Helicopter Society 4th Decennial Specialist's Conference on Aeromechanics*, San Franscisco, CA, 2004.

3. Kenneth S. Brentner and F. Farassat. Modeling aerodynamically generated sound of helicopter rotors. *Progress in Aerospace Sciences*, 39:83–120, 2003.

4. F. Farassat and H. Tadghighi. Can shock waves on helicopter rotors generate noise? A study of the quadrupole source. In *American Helicopter Society 46th Annual Forum Proceedings*, Washington, D.C., 1990.

5. Ann P. Dowling and J. E. Ffowcs Williams. *Sound and Sources of Sound*. Ellis Horwood Publishers, Chichester, West Sussex, England, 1983.

6. Wayne Johnson. A comprehensive analytical model of rotor aerodynamics and dynamics, part i: Analytical development. NASA TM 81182, June 1980.

7. W.M. Chan P.G. Buning, K.J. Renze, D.L. Sondak, I.-T. Chiu, and J.P. Slotnick. *OVERFLOW User's Manual, Version 1.6ab, 26 January 1993*. NASA Ames Research Center, Moffett Field, CA, Jan. 1993.

8. D.C. Jespersen, T.H. Pulliam, and P.G. Buning. Recent enhancements to OVERFLOW. In *AIAA-97-0644, AIAA 35th Aerospace Sciences Meeting*, Reno, NV, Jan. 1997.

9. R. Sarjeant, M. Frecker, and F. Gandhi. Optimal design of a smart conformable rotor airfoil. In *Proceedings of the 2002 ASME International Mechanical Engineering Congress & Exposition (Winter Annual Meeting)*, New Orleans, Louisiana, November 2002.

10. Anna-Maria R. McGowan, editor. *Smart Structures and Materials 2002: Industrial and Commercial Applications of Smart Structures Technologies*. NASA Langley Research Ctr., Hampton, VA, March 2002.